Article

Mechanical Performance of a Node-Reinforced Body-Centered Cubic Lattice Structure: An Equal-Strength Concept Design

Zeliang Liu [1,2,3,]*, Rui Zhao [2], Chenglin Tao [2], Yuan Wang [2] and Xi Liang [1,2]

1 Hebei Key Laboratory of Mechanical Reliability for Heavy Equipments and Large Structures, Yanshan University, Qinhuangdao 066004, China; ysulxi@163.com

2 School of Civil Engineering and Mechanics, Yanshan University, Qinhuangdao 066004, China; zhaorui20211015@163.com (R.Z.); taochenglin@stumail.ysu.edu.cn (C.T.); wy36992021@163.com (Y.W.)

3 State Key Laboratory of Metastable Materials Science and Technology, Yanshan University, Qinhuangdao 066004, China

* Correspondence: liuzeliang@ysu.edu.cn

Abstract: Lattice structures are characterized by a light weight, high strength, and high stiffness, and have a wide range of applications in the aerospace field. Node stress concentration is a key factor affecting the mechanical performance of lattice structures. In this paper, a new equal-strength body-centered cubic (ES-BCC) lattice structure was additively manufactured using 316L stainless steel via selective laser melting (SLM). The results of a mechanical compression test and finite element analysis revealed that the failure location of the ES-BCC structure changed from the nodes to the center of the struts. At the same density, the energy absorption, elastic modulus, and yield strength of the ES-BCC structure increased by 11.89%, 61.80%, and 53.72% compared to the BCC structure, respectively. Furthermore, the change in angle of the ES-BCC structure achieves significant changes in strength, stiffness, and energy absorption to meet different design requirements and engineering applications. The equal-strength concept design can be applied as a general design method to the design of other lightweight energy-absorbing lattice structures.

Keywords: lattice structure; equal-strength design; compressive response; energy absorption

1. Introduction

Lattice structures are structures constructed by combining one or more structural cytons in a periodic array. Due to their superior characteristics of light weight, high strength, high stiffness, energy absorption, vibration damping, and heat and noise insulation, they are widely used in lightweight design, aerospace, biomedicine, and automotive ships [1–3]. The advancement of additive manufacturing technology has advantages in the design and processing of lattice structures, which has greatly promoted the development of such structures and made them a hotspot for lightweight structure research in the aerospace and aviation fields [4].

The current reported lattice structures include body-centered cubic (BCC), face-centered, simple cubic, octet, diamond, rhombic dodecahedron, pyramidal, octet-truss, triply periodic minimal surface, and hybrid structures [5–11]. Besides the materials used for manufacturing structures, the shape and geometrical parameters of the lattice structure determine its mechanical properties, i.e., the number, orientation, and diameter of the struts [12]. Lattice structures have been classified into tensile-dominated and bending-dominated types [13–15]. Therefore, the deformation mechanism of the struts under load has been considered as determining the mechanical performance of the structure [16,17]. However, almost all of the currently reported stress concentration is often initiated at the nodes, which leads to faster crack initiation and failure [18–20].

Some studies improve the mechanical properties of lattice structures through the node design. A novel BCC lattice structure with tapered struts was designed to reduce the stress

concentration at the nodes [6]. The results show that the structure fracture location changed from the nodes to the tapered strut center, and the elastic modulus was increased by 67%. A new graded-strut body-centered cubic structure was obtained by replacing node right angles with node fillets [21,22]. In the filleted structure, strut failure initiated near the end of the fillet, and the compressive modulus and yield strength were increased by at least 38.20% and 34.12%, respectively. Taking inspiration from a crystal structure, a BCC structure with atoms as reinforced nodes and atomic bonds as connected struts has been manufactured [23], and the yield strength and collapse strength were increased by 12.31% and 31.19%, respectively. Although experience-based node reinforcement design improves the mechanical performance of structures, it lacks theoretical support and is difficult to widely apply.

In the present work, a new equal-strength body-centered cubic (ES-BCC) lattice structure was proposed. The material is additively manufactured with 316L stainless steel via the SLM process. The deformation mode, elastic modulus, yield strength, and energy absorption of the ES-BCC structure were investigated using numerical simulation and compression tests and compared with the BCC structure. The equal-strength design of the struts can effectively improve the mechanical properties of the structure, which provides a new idea for the design of lightweight energy-absorbing structures in the aerospace field.

2. Materials and Methods

2.1. Design of ES-BCC Structure

The ES-BCC structure was designed based on the equal-strength concept of the BCC structure. Figure 1 shows the schematic diagram of the BCC structure under axial compression: the shaded portion indicates that the bottom of the structure is a fixed constraint. The BCC lattice structure, as shown in Figure 1a, contains unit cells with bottom dimensions of $L \times L$ and the height H. The eight struts surrounding the node are taken as the analysis module, as shown in Figure 1b. Assuming that the compression load is F, since the structure is geometrically symmetric, any strut near the node can be taken for force analysis, which is simplified into a cantilever beam structure. The strut AB is taken for force analysis, as shown in Figure 1c.
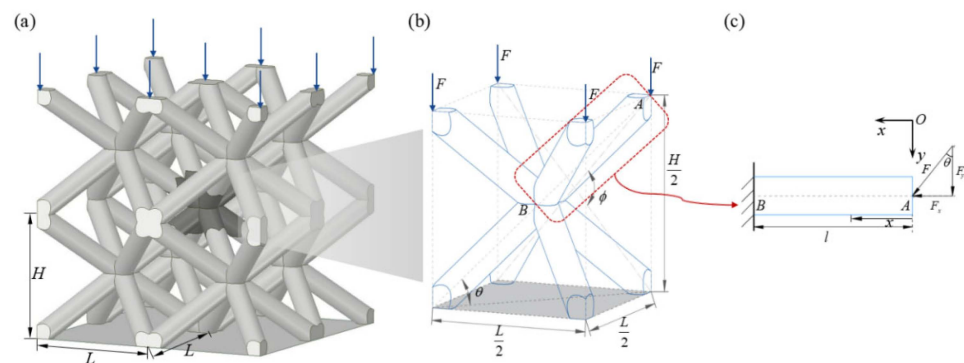
Figure 1. Schematic diagram of the BCC structure under axial compression. (**a**) The BCC lattice structure; (**b**) analysis module; (**c**) simplified analysis of the force on the struts.

Decomposing the load F, the axial and tangential forces on the strut can be obtained as:

$$\begin{cases} F_x = F \sin \theta \\ F_y = F \cos \theta \end{cases} \tag{1}$$

where θ is the angle between the bottom surface and the structural strut.

Under combined compression-bending deformation, the stress can be represented by:

$$\sigma(x) = \frac{F_x}{A(x)} + \frac{M(x)}{W_z(x)} \tag{2}$$

For circular cross-section struts, $A(x) = \frac{\pi d^2(x)}{4}$ is the cross-sectional area at x, $M(x) = F_y x$ is the bending moment at x, and $W(x) = \frac{\pi d^3(x)}{32}$ is the bending section coefficient.

Letting the stress at any x be equal to the allowable stress of the base material, we have:

$$\sigma_{\max} = [\sigma] = \begin{cases} \frac{4F \sin\theta}{\pi d_0^2} (x = 0) \\ \frac{4F \sin\theta}{\pi d_1^2} + \frac{32F \cos\theta l}{\pi d_1^3} (x = l) \end{cases} \tag{3}$$

where d_0 is the initial diameter (diameter at the center of struts), and d_1 is the maximum diameter (diameter at nodes), $l = \sqrt{2L^2 + H^2}/4$. From Equation (3), we have:

$$F = \frac{\pi d_0^2 [\sigma]}{4 \sin\theta} \tag{4}$$

Substituting Equation (4) into $\sigma(x) = [\sigma]$, the function of the strut diameter can be given as:

$$d^3(x) - d_0^2 d(x) = 8 \cot\theta d_0^2 x \tag{5}$$

Equation (5) is the design formula for the ES-BCC structure. Obviously, the diameter of the strut is related to d_0 and θ.

As shown in Figure 1b, ϕ is the angle between the struts in the front view of the structure. From the geometric relationship, the relationship between ϕ and θ can be obtained:

$$\sin\theta = \frac{\tan\frac{\phi}{2}}{\sqrt{2 + \tan^2\frac{\phi}{2}}} \tag{6}$$

ES-BCC unit cell structures with d_0 = 0.3 mm are shown in Table 1. Since a non-smooth transition at the center of the strut would result in stress concentration, a rounded corner transition with R = 3 mm was performed in the actual modeling. As shown in Table 1, the shapes of the strut profiles determined using Equation (5) are similar, with differences only in the size of the diameters at each location. For structures with ϕ of 75°, 90°, 105°, and 120°, the minimum diameters of the struts after adding rounded corners are 0.86, 0.76, 0.69, and 0.63 mm when d_0 is 0.30 mm, respectively.

Table 1. The ES-BCC unit cell structure with d_0 = 0.3 mm.

ϕ	θ	$d(x)$	Strut Profile	Unit Cell Model
75°	27.37°	$d^3(x) - 0.09d(x) = \frac{18\sqrt{2}}{25(\sqrt{3}-1)}x$		
90°	35.26°	$d^3(x) - 0.09d(x) = \frac{18\sqrt{2}}{25}x$		
105°	42.66°	$d^3(x) - 0.09d(x) = \frac{18\sqrt{2}}{25(2+\sqrt{6}-\sqrt{2}-\sqrt{3})}$		
120°	50.77°	$d^3(x) - 0.09d(x) = \frac{18\sqrt{6}}{75}x$		
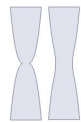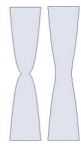
2.2. Relative Density

The ratio of the solid volume of the structure to the volume of the quadrilateral filled by the structure is the relative density of the lattice structure. When filling the lattice structure into the cube, the ends of each strut are partially truncated in the x, y, and z directions, and a schematic diagram of the intercepted structural strut dimensions is shown in Figure 2.
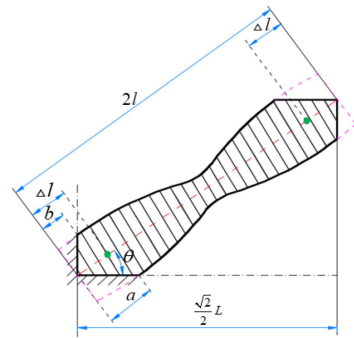
Figure 2. Schematic diagram of the geometric dimensions of the strut.

The distance between the nodes of the force can be expressed by $2(l - \Delta l)$. If the strut is uniform, then $\Delta l = \frac{a+b}{2} = \frac{d}{4}\left(\tan\theta + \frac{1}{\tan\theta}\right)$, where d is the strut diameter. For the new design structures, the diameter d is a function of x, and d is approximated as $(d_0 + d_1)/2$. Thus, we obtain:

$$\Delta l = \frac{d_0 + d_1}{8}\left(\tan\theta + \frac{1}{\tan\theta}\right) \tag{7}$$

here, d_0 is the minimum diameter after adding rounded corners and d_1 is the maximum diameter.

As shown in Figure 2, the volume of the variable-section strut of the $2l$ segment is $V_1 = 2\int_0^l \pi r^2(x)dx$.

From the above analysis, the volume of the $2(l - \Delta l)$-segment strut can be obtained as:

$$V_2 = 2\int_0^{l-\Delta l} \pi r^2(x)dx \tag{8}$$

Since each strut of the structure is partially truncated, the volume of the Δl-segment strut is approximated as $V_{\Delta l} = (V_1 - V_2)/8$. The unit cell volume can be obtained as follows:

$$V = 8(V_2 + 2V_{\Delta l}) \tag{9}$$

The relative density can be obtained with rectification as follows:

$$\bar{\rho} = \frac{V}{L^2 H} \tag{10}$$

2.3. Specimen Fabrication

The bottom surface dimensions of the ES-BCC unit cell structure are $L \times L$, taking $L = 6$ mm, and the height H is related to ϕ. The ES-BCC structure is named according to ϕ to facilitate later analysis. For example, a lattice structure with $\phi = 75°$ is named an A075 structure.

The specimens were fabricated using a selective laser melting (SLM) process, and 316L stainless steel was selected as the fabrication material. To eliminate the influence of the specimen printing direction, all specimens were fabricated along the direction of the experimental load. The overall dimensions of the structures were 30 mm × 30 mm × 30 mm. To compare the mechanical properties of the ES-BCC structures with those of the original BCC lattice structure, the conventional BCC lattice structure (strut diameter $d = 1.025$ mm) was fabricated with the same dimensions and relative density as the A090 structure. In order to avoid errors in the experimental process, two specimens were prepared for all

lattice structures. The specimens are shown in Figure 3. Table 2 shows 316L stainless steel's chemical composition [24].
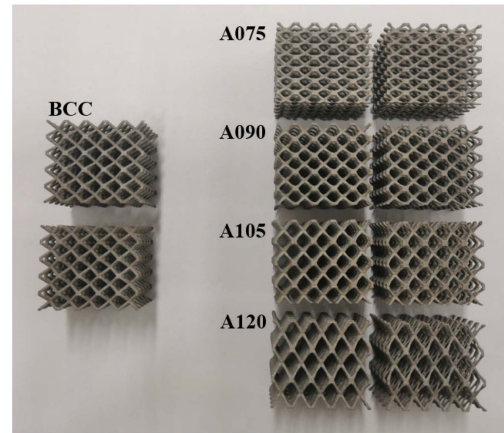
Figure 3. Fabricated lattice structure specimens.

Table 2. 316L stainless steel's chemical composition (%) [24].

C	Si	Mn	S	P	Cr	Ni	Mo	Fe
0~0.03	0~1.0	0~2.0	0~0.03	0~0.045	16.5~18.5	10.0~13.0	2.0~3.0	Balance

2.4. Experimental Procedure

Quasi-static tests were performed on the specimens using an Instron 5982 universal material testing machine, including tensile and compressive. The quasi-static compression test setup is shown in Figure 4a. The loading speed was set to 2 mm/min. For compression testing, the loading was stopped at the densification stage or 25 mm displacement. For tensile testing, the loading was stopped when the specimen fractured. The force and displacement are automatically recorded by the data acquisition system. A DSLR camera Canon 80 D was used to record the entire process of the experiment in real time. The tensile stress–strain curves of the additive manufacturing 316L stainless steel specimens are shown in Figure 4b. The mechanical properties shown in Table 3 are similar to those in reference [25,26], which were used in the subsequent numerical simulations.
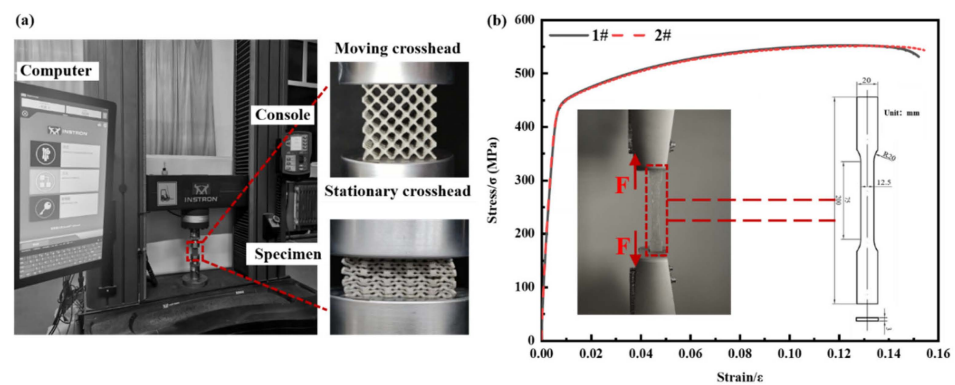
Figure 4. The quasi-static tests. (**a**) Instron testing machine; (**b**) stress–strain curves of the additive manufacturing 316L stainless steel specimens.

Table 3. The mechanical property parameters of 316L stainless steel.

Elastic Modulus (GPa)	Density (g/cm^3)	Poisson's Ratio	Yield Stress (MPa)	Ultimate Stress (MPa)
67	7.59	0.3	443.63	551.63

2.5. Finite Element Modeling

The modeling, meshing, and solving were performed using the CAD, HyperMesh 2021, and LS-DYNA R11.1.0 software. The finite element model is shown in Figure 5a. The effect of the strain rate is not considered in the quasi-static compression tests. To simulate the upper and lower indenters in the compression test, rigid plates are placed and meshed with shell elements, and the lattice structure is meshed with solid elements (C3D8R). The top rigid plate was loaded with displacement at a constant rate of 1 m/s [27,28], which was to improve the computational efficiency of the numerical simulation [29–32], with a compression displacement of 25 mm, and the bottom rigid plate was completely fixed. The static friction coefficient between the lattice structure and indenters is 0.3 [33,34].
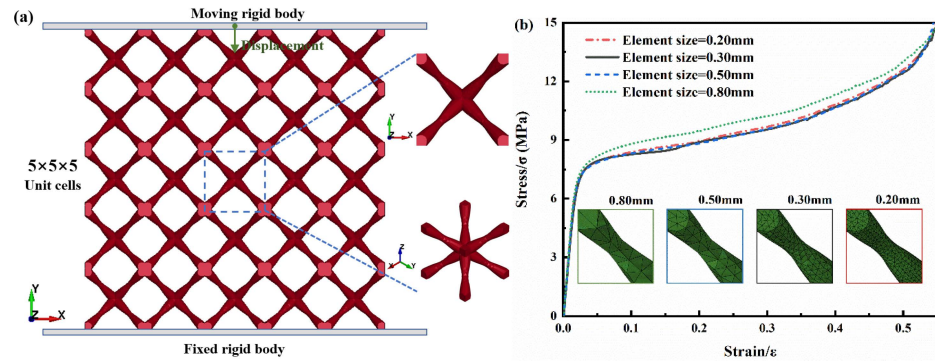
Figure 5. Numerical simulation. (**a**) Finite element model setup; (**b**) mesh convergence test.

The mesh convergence test was conducted to reduce the influence of the mesh element size on the stress–strain curve, as shown in Figure 5b. The element sizes were 0.2, 0.3, 0.5, and 0.8 mm, respectively. The stress–strain curve of the finite element model with an element size of 0.8 mm had large deviations from those of the other sizes, and the error between the results of element sizes of 0.2, 0.3, and 0.5 mm was very small. Therefore, elements with a grid size of 0.3 mm were used for subsequent simulation calculations.

3. Results and Discussion

3.1. Morphological Characteristics

The masses of all specimens were obtained by weighing them, and the relative densities were calculated. Figure 6 shows the design values, theoretical values, and measured values of the relative density of the ES-BCC structures. The relative density of all specimens was smaller than the design value, the maximum error was 6.2%, and the relative density error between the design and theoretical values was less than 6.9%. The main reason for errors would have been rounded transitions, approximately calculated volumes, defects, and residual powder particles.
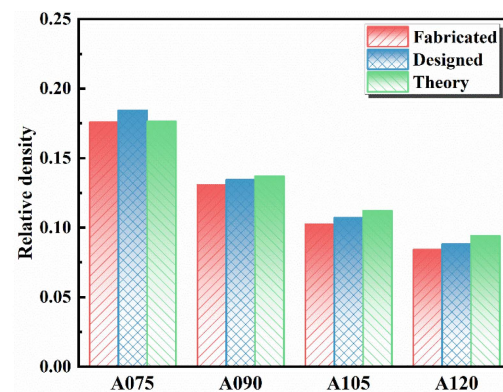
Figure 6. Comparison of relative density of specimens, design models, and theoretical values.

Scanning electron microscopy (SEM) was used to assess the manufacturing quality of the experimental specimens. As shown in Figure 7, the surface of each strut was rough. The adhesion of partially melted powder particles can be observed, especially at the nodes and below the struts. Moreover, porosity defects were observed on the struts. At the intersection of the struts, small-angle structures had more residual powder particles than large-angle structures. Furthermore, porosity defects might also exist inside the struts of the lattice structure.
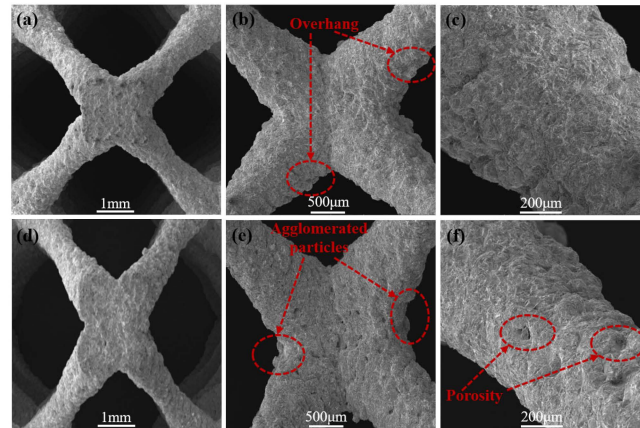
Figure 7. SEM images of ES-BCC structures. (**a**–**c**) A090; (**d**–**f**) A120.

3.2. Mechanical Properties

The compressive stress–strain curves of the A090 structure and the BCC lattice structure were compared, as shown in Figure 8. The simulation curves are in good agreement with the experimental results, especially in the initial phases. Under quasi-static compression, the lattice structure exhibited the following deformation responses: an initial linear elastic phase, a plastic plateau phase where the stress remained constant, and a densification phase where the stress sharply grew. The pentagram in the Figure 8 represents the starting point of the structure into the densification phase. The compressive stress–strain curves of the A090 and BCC lattice structures had the same trend, but at the same strain, the former's stress exceeded the latter.
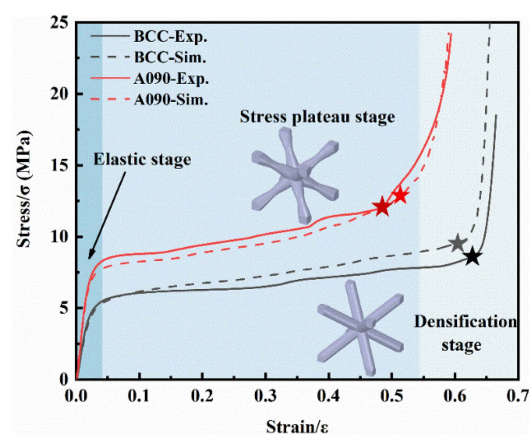
Figure 8. Compressive stress–strain curves: A090 and BCC lattice structures.

The deformation behavior can directly reflect the damage failure mode. Figure 9 depicts the deformation process of the lattice structure in compression tests and simulations. When the strain reached 40%, both the A090 and BCC lattice structures had significant deformation on the diagonal struts, and the center of the structure showed local densification. Struts in various areas exhibited different deformation patterns, with the external struts producing tensile deformation and the internal struts producing buckling deformation.

The BCC lattice structure was deformed uniformly in the compression process. The overall stress distribution of the structure was not uniform, and at the nodes of the struts, stress concentration was observed. However, the A090 structure was the first to show bending deformation and compaction at the center of the strut where it made contact with the upper and lower plates. The rest of the layers deformed uniformly. During the compression process, the stress distribution of the A090 structure was more uniform, and the damage failure location was at the center of the strut.
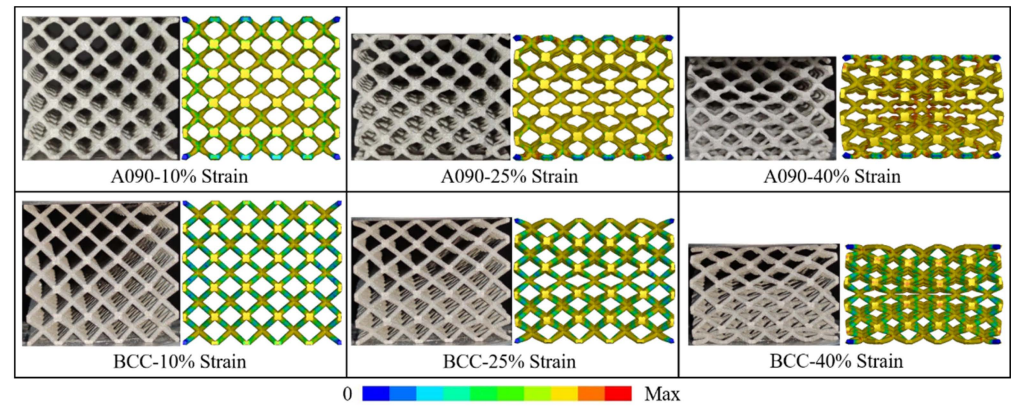
Figure 9. The compression deformation process of the lattice structures.

To quantitatively describe the mechanical properties and energy absorption characteristics of the ES-BCC structures, the elastic modulus (E), yield strength (σ_y), and energy absorption (EA) were compared. The elastic modulus was defined as the slope of the initial linear elastic segment (about 1–3% of the strain). The yield strength was defined as the stress at the point where the stress–strain curve intersected a straight line whose slope equaled the elastic modulus and passed through the 0.2% strain [35]. The energy absorption of a lattice structure can be represented by the energy absorption per unit volume as the area under the compressive stress–strain curve:

$$EA = \int_0^{\varepsilon_d} \sigma(\varepsilon)d\varepsilon \tag{11}$$

where $\sigma(\varepsilon)$ and ε are the stress and strain during compression, respectively, and ε_d is the maximum strain when the structure is compressed to the densification stage [36]. Table 4 shows the densification strains of the experimental and simulated compression stress–strain curves. It can be observed that the densification strain increases with ϕ. The ε_d of the BCC lattice structure exceeded that of the A090 structure, consistent with the compressive stress–strain curves shown in Figure 9.

Table 4. Structural parameters of lattice structures.

Lattice Type		BCC	A075	A090	A105	A120
Relative density	Exp.	0.1265	0.1757	0.1307	0.1023	0.0841
	Sim.	0.1344	0.1842	0.1344	0.1070	0.0880
Densification strain	Exp.	0.6288	0.4492	0.4848	0.5356	0.5864
	Sim.	0.6075	0.4327	0.5142	0.5283	0.5708

Table 5 compares the mechanical properties of the structures under study in compression tests and simulations. The discrepancies among the elastic moduli, yield strengths, and energy absorptions were within 10.5%, 1.2%, and 2.6%, respectively, proving the reliability of the numerical simulation. The elastic modulus, yield strength, and *EA* of the A090 structure outperformed those of the BCC lattice structure by 61.80%, 53.72%, and 11.89%, respectively.

Table 5. The elastic modulus, yield strength, and energy absorption of lattice structures.

Lattice Type	Elastic Modulus (MPa)			Yield Strength (MPa)			Energy Absorption (J/cm^3)		
	Exp.	Sim.	DEV$_{ES}$	Exp.	Sim.	DEV$_{ES}$	Exp.	Sim.	DEV$_{ES}$
A090	373.58	345.46	−7.53%	6.69	6.61	−1.20%	4.68	4.80	2.56%
BCC	238.34	213.51	−10.42%	4.28	4.30	0.47%	4.21	4.29	1.90%

Note: Deviation DEV$_{ES}$ = (Sim. − Exp.)/Exp. × 100%.

3.3. Influence of ϕ

At the initial diameter d_0 = 0.3 mm, the effect of ϕ on the mechanical properties of the ES-BCC structures was studied, as shown in Figure 10. The stress was initially concentrated at the center of the struts of the top and bottom cell layers and propagated to the adjacent layers with the ongoing crush. At a strain of 40%, significant densification occurred at the center of the structure. The smaller ϕ was, with more crystal cells and a higher relative density resulting in faster densification of the structure during compression, the more uniform the stress distribution was. It was also noticed that the collapse began at the top and bottom cell layers, followed by the middle layer, and finally the adjacent two layers began to collapse. The specimens did not produce fracture damage during compression.
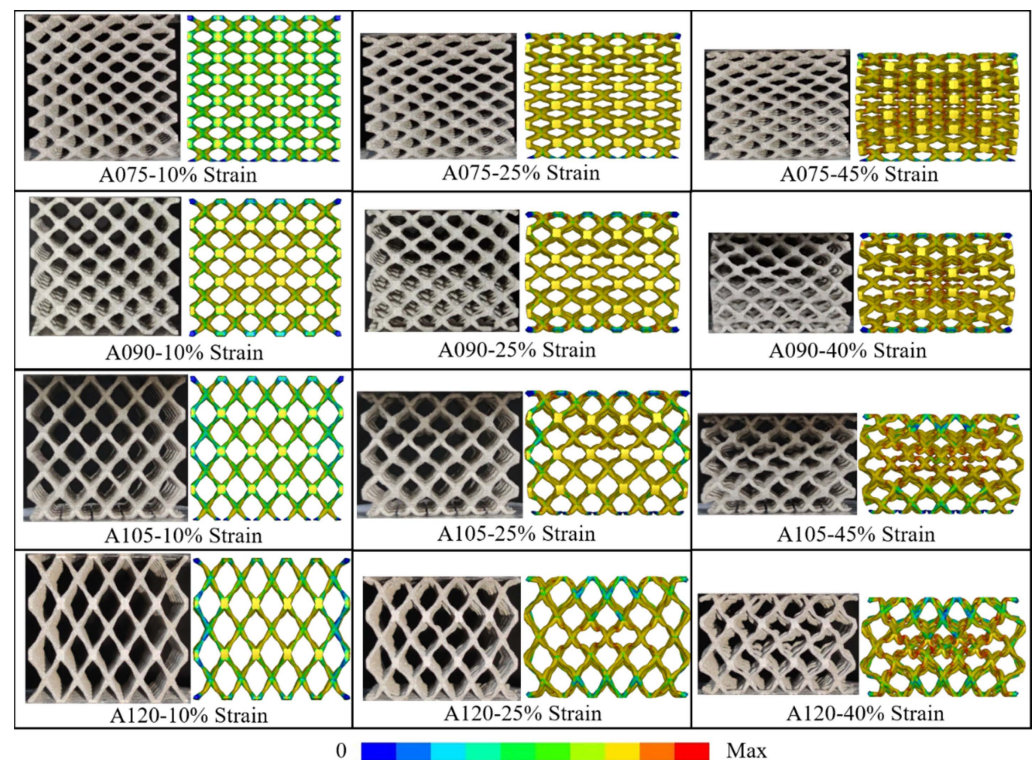
Figure 10. Stress-strain curve of 316L stainless steel material.

The compressive stress–strain curves of ES-BCC structures with different ϕ are presented in Figure 11. It demonstrates the typical stress–strain behavior of lattice structures with three characteristic regions consisting of a linear elastic region, plateau region, and densification region. The change in ϕ did not affect the general trend of the stress–strain curve but at the same strain, the stress decreased with an increasing ϕ. The smaller the angle, the greater the elastic modulus, yield strength, and energy absorption, but the influence of mass is not taken into account.
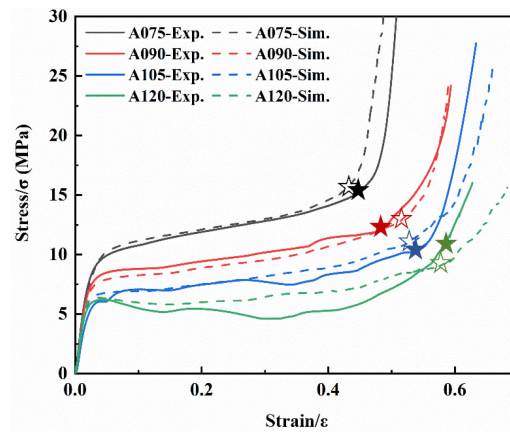
Figure 11. The stress–strain curves of ES-BCC structures with different ϕ.

The mechanical properties of ES-BCC structures at different ϕ values were further evaluated by calculating their relative elastic modulus ($E_{\bar{\rho}}$), relative yield strength ($\sigma_{\bar{\rho}}$), and specific energy absorption (*SEA*) [37,38]. The calculation formula is as follows:

$$E_{\bar{\rho}} = \frac{E}{\bar{\rho}} \tag{12}$$

$$\sigma_{\bar{\rho}} = \frac{\sigma_y}{\bar{\rho}} \tag{13}$$

$$SEA = \frac{EA}{\rho} = \frac{\int_0^{\varepsilon_d} \sigma(\varepsilon)d\varepsilon}{\rho} \tag{14}$$

where ρ is the density of the lattice structure.

Figure 12 shows the mechanical properties of ES-BCC structures with different ϕ. The larger ϕ, the greater the relative elastic modulus, relative yield strength, and specific energy absorption. When the ϕ of the structure increased from 75° to 120°, the relative elastic modulus grew from 2.19 to 3.64 GPa (i.e., by 66.21%), the relative yield strength grew from 44.34 to 65.87 MPa (i.e., by 48.56%), and the SEA increased from 3.89 to 5.59 J/g (i.e., by 43.70%). Therefore, the A120 structure had a superior elastic modulus, yield strength, and EA at the same relative density. Mainly due to the increase in angle, the compression force of the structure increases and the bending force decreases.
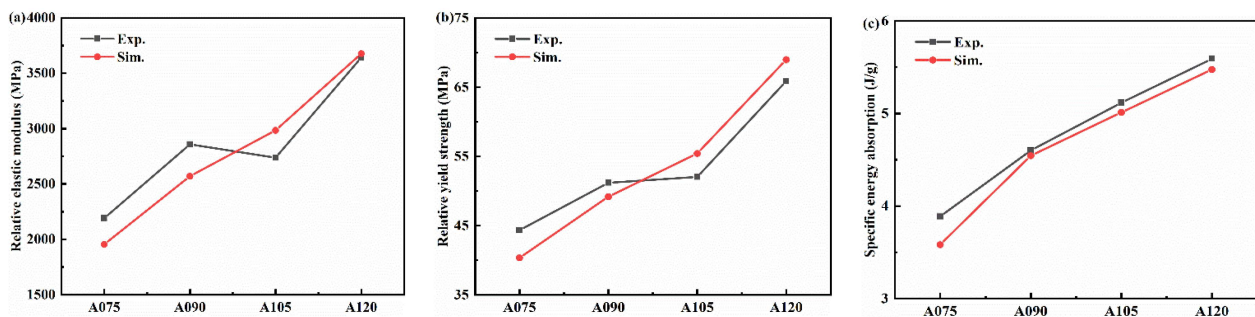
Figure 12. The mechanical properties of ES-BCC structures with different ϕ: (**a**) relative elastic modulus; (**b**) relative yield strength; (**c**) specific energy absorption.

3.4. Gibson–Ashby Model Prediction

The Gibson–Ashby (GA) model [39] is a classical model theory based on cubic porous structures simplified by cubic struts. It uses the geometric mechanics method to link porous materials' mechanical properties and can effectively predict their tensile and compressive properties, such as the elastic modulus, tensile and compressive strength, and energy absorption. The normalized elastic modulus and normalized yield strength of the lattice

structure can be characterized by power functions of the relative density via the GA equations as follows:

$$\frac{E}{E_s} = C_1 \bar{\rho}^{n_1} \tag{15}$$

$$\frac{\sigma_y}{\sigma_s} = C_2 \bar{\rho}^{n_2} \tag{16}$$

where E and σ_y are the compressive modulus and yield strength of the lattice structure, respectively, E_s and σ_s are the elastic modulus and yield strength of the matrix material, respectively, while the coefficient C and the exponent n characterize the geometry of the unit cell. The exponent reflects the mechanical properties of the lattice structure better than the coefficient because the functional relationship follows power function characteristics. Structures with different relative densities were analyzed with a d_0 of 0.15, 0.20, 0.25, and 0.30 mm. The fitted curves of the GA model for the E and σ_y of the lattice structures are shown in Figure 13.
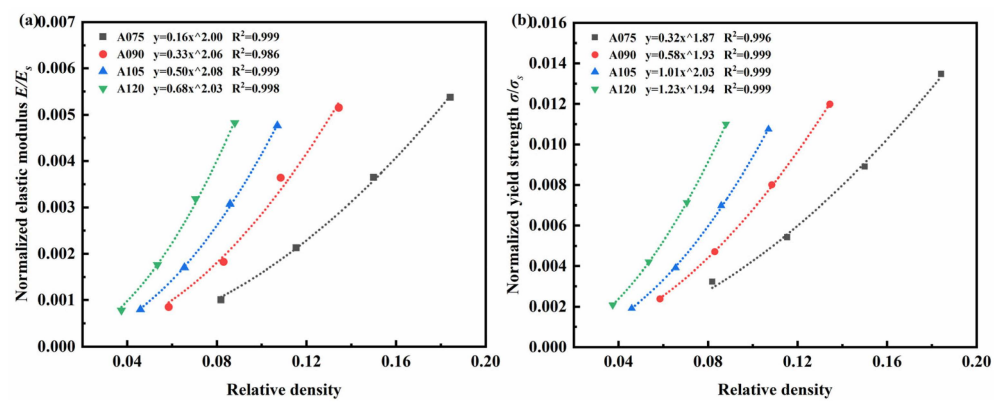
Figure 13. Mechanical properties–relative density fitting curves of lattice structures. (**a**) E/E_s; (**b**) σ_y/σ_s.

As shown in Figure 13, the E and σ_y of the lattice structures increased as $\bar{\rho}$ increased. The mechanical properties improved significantly with increasing ϕ, while the E and σ_y of the A120 structure significantly exceeded those of other lattice structures with the same relative density. This substantiates the design concept of high-strength and high-stiffness lattice structures.

The fitted parameters of the GA model for the mechanical properties of ES-BCC structures are listed in Table 6. Due to the large difference in the exponents of lattice structures with various geometric configurations [40], according to the Maxwell criterion [41], lattice structures are classified as tensile- or bending-dominated based on their deformation forms. Bending- and tensile-dominant deformation structures have a normalized elastic modulus index n_1 close to 2 and 1, respectively, and a normalized yield strength index n_2 close to 1.5 and 1, respectively. Notably, the indices n_1 and n_2 of the ES-BCC structures were close to 2 and 1.5, respectively. Therefore, the ES-BCC structures under study exhibited bending-dominated deformation under quasi-static compression, which were more stable in the plateau phase and had higher energy absorption [42].

Table 6. The fitting parameters of the GA model for the mechanical properties of ES-BCC structures.

Lattice Type	Normalized Elastic Modulus			Normalized Yield Strength		
	C_1	n_1	R^2	C_2	n_2	R^2
A075	0.16	2.00	0.999	0.32	1.87	0.996
A090	0.33	2.06	0.986	0.58	1.93	0.999
A105	0.50	2.08	0.999	1.01	2.03	0.999
A120	0.68	2.03	0.998	1.23	1.94	0.999

3.5. Theoretical Analysis

3.5.1. Equivalent Elastic Modulus

Assume that the lattice structure is only subjected to an axial compression load *F*, as shown in Figure 14. The load *F* is decomposed into the axial force F_x and tangential force F_y, and the strut displacement can be decomposed into axial displacement δ_x and tangential displacement δ_y.
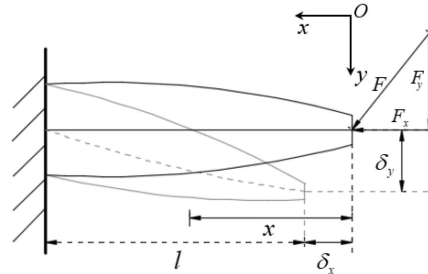
Figure 14. The force schematic of the 1/2 variable-section strut.

The axial displacement δ_x of the strut is:

$$\delta_x = \int_0^l \frac{F_x}{EA(x)} dx = \int_0^l \frac{4F \sin\theta}{E\pi d^2(x)} dx \tag{17}$$

where *E* is the elastic modulus of the structural material.

Tangential displacement δ_y is caused by the combined action of the bending moment and shear. The tangential displacement can be obtained using the unit load method as:

$$\delta_y = \int_0^l \frac{\overline{M}M(x)}{EI(x)} dx + \int_0^l \frac{K_s F_y}{GA(x)} dx \tag{18}$$

where $\overline{M} = x$ is the bending moment under unit load; $K_s = 10/9$ is the shear coefficient for a circular section; $G = E/2(1+\mu)$ is the shear modulus; and $I(x) = \frac{\pi d^4(x)}{64} = \frac{\pi r^4(x)}{4}$ is the moment of inertia at *x*.

Let the displacement of the unit cell in the compression direction be δ. Projecting the axial and tangential displacements onto the force direction, we can obtain:

$$\delta = 4(\delta_x \sin\theta + \delta_y \cos\theta) \tag{19}$$

The equivalent elastic modulus can be expressed as:

$$E_e = \frac{\sigma_e}{\varepsilon_e} \tag{20}$$

where $\sigma_e = \frac{4F}{L^2}$ is the equivalent stress, and $\varepsilon_e = \frac{\delta}{H}$ is the equivalent strain, collated to obtain:

$$E_e = \frac{4FH}{L^2 \delta} \tag{21}$$

3.5.2. Equivalent Yield Strength

When the lattice structure is subjected to axial compression, the combined action of the axial force and bending moment is applied to the variable-section struts, resulting in combined compression-bending deformation, eventually causing the damage failure of the structure. Struts are prone to buckling under compressive loading, but the struts in the ES-BCC structure studied in this paper do not satisfy the slender rod condition, so the buckling effect is not considered. According to the compression test, it is found that the plastic yielding damage of the structure was first produced on the tensile side, so taking the tensile stress surface as the plastic damage failure criterion surface, the stress expression at *x* is as follows:

$$\sigma(x) = \frac{M(x)}{W(x)} - \frac{F_x}{A(x)} \qquad (22)$$

At a maximum x, i.e., when $x = l$, the maximum value of stress is observed. Making $\sigma(x)_{max}$ equal to the yield strength of the substrate, we obtain:

$$F_{max} = \frac{\sigma(l)}{\frac{32 \cos \theta l}{\pi d^3(l)} - \frac{4 \sin \theta}{\pi d^2(l)}} \qquad (23)$$

Then, the plastic damage strength is:

$$\sigma_y = \frac{4 F_{max}}{L^2} \qquad (24)$$

When the lattice structure undergoes plastic failure, it can be regarded as reaching the yield state, and the plastic damage strength at this time is the equivalent yield strength.

3.5.3. Elastic Modulus and Yield Strength Analysis

The parameters E and σ_y of ES-BCC structures with different ϕ can be obtained by applying the theoretical prediction equation. As shown in Figure 15, the theoretical values of the A075 and A090 structures are smaller than the experimental and simulated values because in the theoretical prediction, the calculation object is the unit cell structure with direct contact between the top layer and the indenter, but in the actual compression process, the top and bottom layers of the structure are the first to produce damage failure, while the inner unit cell is more constrained and bears part of the load. The theoretical values of the A105 and A120 structures are larger than the experimental and simulated values, probably because the struts are longer. The struts are prone to buckling and combined bending and torsional deformation at the nodes, while the influence of strut buckling is not considered in the theoretical calculations.
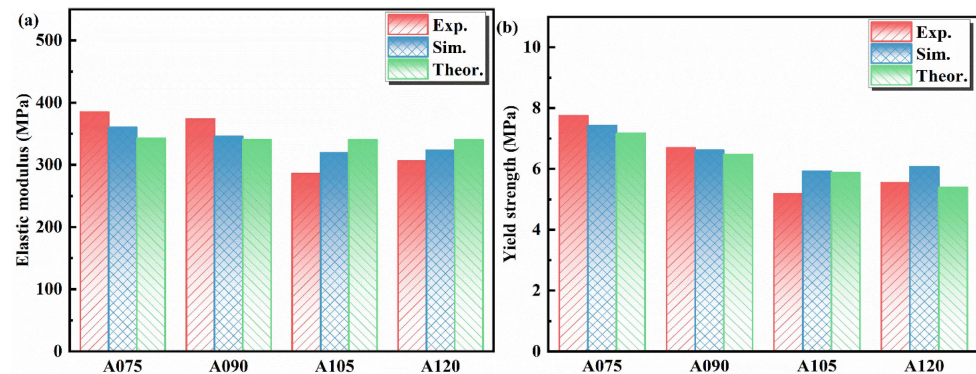
Figure 15. Comparison of the mechanical properties of ES-BCC structures. (**a**) E; (**b**) σ_y.

Table 7 shows the E and σ_y values of ES-BCC structures with different ϕ values. The discrepancies in E between the experimental and simulated results ranged from -7.52% in the A090 structure to 11.73% in the A105 structure, while those in σ_y ranged from -4.13% for the A075 structure to 14.26% for the A105 structure. The deviations between the experimental and simulated or theoretical values of the A105 structure were the largest because of the unavoidable processing defects in the specimens. However, its simulated results were more consistent with the theoretical ones. The discrepancies between the experimental and theoretical values of E and σ_y for the ES-BCC structures were within 18.93 and 13.29%, proving that the theoretical model could predict E and σ_y of the ES-BCC structures effectively.

Table 7. Mechanical properties of ES-BCC structures: experimental, simulated, and theoretical.

Lattice Type	Elastic Modulus (MPa)					Yield Strength (MPa)				
	Exp.	Sim.	Theor.	DEV$_{ES}$	DEV$_{ET}$	Exp.	Sim.	Theor.	DEV$_{ES}$	DEV$_{ET}$
A075	384.84	360.05	342.66	−6.44%	−10.96%	7.75	7.43	7.17	−4.13%	−7.48%
A090	373.58	345.46	340.66	−7.52%	−8.81%	6.69	6.61	6.47	−1.20%	−3.29%
A105	285.85	319.38	339.95	11.73%	18.93%	5.19	5.93	5.88	14.26%	13.29%
A120	306.21	323.60	340.09	5.68%	11.06%	5.55	6.07	5.39	9.37%	−2.88%

Note: DEV$_{ES}$ = (Sim. − Exp.)/Exp. × 100%; DEV$_{ET}$ = (Theor. − Exp.)/Exp. × 100%.

4. Conclusions

In this study, an equal-strength concept was proposed for building novel lattice structures, and a new BCC lattice structure, equal-strength body-centered cubic (ES-BCC), is designed, which can be applied as a lightweight structure in the aerospace field. The mechanical properties of the designed structure were analyzed using experiments and finite element analysis, and the main conclusions are as follows:

(1) ES-BCC lattice structures based on the equal-strength concept were designed to reduce the node stress concentration effectively. The yield position of the BCC lattice structures changed from the node region to the center of strut. The elastic modulus, yield strength, and energy absorption of the A090 structure were improved by 61.80%, 53.72%, and 11.89% compared to the BCC structure, respectively.

(2) The ES-BCC lattice structures all exhibited bending-dominated deformation. A larger ϕ corresponded to a higher relative elastic modulus, relative yield strength, and SEA. Those of the A120 structure reached 3.64 GPa, 65.87 MPa, and 5.59 J/g, respectively, outperforming those of the A075 structure by 66.21, 48.56, and 43.70%, respectively.

(3) By changing ϕ from 75° to 120°, substantial variations in strength, stiffness, and energy absorption were achieved to meet different design requirements and engineering applications. Thus, small-angle ES-BCC lattice structures can be used in energy-buffering devices, and large-angle ones can meet high-strength requirements.

Author Contributions: Z.L.: conceptualization, methodology, funding acquisition, investigation, writing—review and editing. R.Z.: writing—original draft, software, visualization, validation. C.T.: writing—original draft, software, validation. Y.W.: writing—original draft, validation. X.L.: project administration, writing—review and editing. All authors have read and agreed to the published version of the manuscript.

Institutional Review Board Statement: Not applicable.

Informed Consent Statement: Not applicable.

Data Availability Statement: Data are contained within the article.

References

1. Maconachie, T.; Leary, M.; Lozanovski, B.; Zhang, X.; Qian, M.; Faruque, O.; Brandt, M. SLM lattice structures: Properties, performance, applications and challenges. *Mater. Des.* **2019**, *183*, 108137. [CrossRef]
2. Tao, C.; Wang, Z.; Liu, Z.; Wang, Y.; Zhou, X.; Liang, X.; Li, H. Crashworthiness of Additively Manufactured Lattice Reinforced Thin-Walled Tube Hybrid Structures. *Aerospace* **2023**, *10*, 524. [CrossRef]
3. Alkhatib, S.E.; Karrech, A.; Sercombe, T.B. Isotropic energy absorption of topology optimized lattice structure. *Thin-Walled Struct.* **2023**, *182*, 110220. [CrossRef]
4. Kumar, A.; Collini, L.; Daurel, A.; Jeng, J.-Y. Design and additive manufacturing of closed cells from supportless lattice structure. *Addit. Manuf.* **2020**, *33*, 101168. [CrossRef]
5. Dong, G.; Tang, Y.; Li, D.; Zhao, Y.F. Design and optimization of solid lattice hybrid structures fabricated by additive manufacturing. *Addit. Manuf.* **2020**, *33*, 101116. [CrossRef]

6. Zhao, M.; Zhang, D.Z.; Li, Z.; Zhang, T.; Zhou, H.; Ren, Z. Design, mechanical properties, and optimization of BCC lattice structures with taper struts. *Compos. Struct.* **2022**, *295*, 115830. [CrossRef]

7. Liu, R.; Chen, W.; Zhao, J. A review on factors affecting the mechanical properties of additively-manufactured lattice structures. *J. Mater. Eng. Perform.* **2023**, 1–27. [CrossRef]

8. Park, J.H.; Park, K. Compressive behavior of soft lattice structures and their application to functional compliance control. *Addit. Manuf.* **2020**, *33*, 101148. [CrossRef]

9. Cao, X.; Xiao, D.; Li, Y.; Wen, W.; Zhao, T.; Chen, Z.; Jiang, Y.; Fang, D. Dynamic compressive behavior of a modified additively manufactured rhombic dodecahedron 316L stainless steel lattice structure. *Thin-Walled Struct.* **2020**, *148*, 106586. [CrossRef]

10. Li, Z.; Nie, Y.; Liu, B.; Kuai, Z.; Zhao, M.; Liu, F. Mechanical properties of AlSi10Mg lattice structures fabricated by selective laser melting. *Mater. Des.* **2020**, *192*, 108709. [CrossRef]

11. Guo, X.; Ding, J.; Li, X.; Qu, S.; Hsi Fuh, J.Y.; Lu, W.F.; Song, X.; Zhai, W. Interpenetrating phase composites with 3D printed triply periodic minimal surface (TPMS) lattice structures. *Compos. B Eng.* **2023**, *248*, 110351. [CrossRef]

12. Lee, K.W.; Lee, S.H.; Noh, K.H.; Park, J.Y.; Cho, Y.J.; Kim, S.H. Theoretical and numerical analysis of the mechanical responses of BCC and FCC lattice structures. *J. Mech. Sci. Technol.* **2019**, *33*, 2259–2266. [CrossRef]

13. Li, S.J.; Xu, Q.S.; Wang, Z.; Hou, W.T.; Hao, Y.L.; Yang, R.; Murr, L. Influence of cell shape on mechanical properties of Ti–6Al–4V meshes fabricated by electron beam melting method. *Acta Biomater.* **2014**, *10*, 4537–4547. [CrossRef] [PubMed]

14. Eckel, Z.C.; Zhou, C.; Martin, J.H.; Jacobsen, A.J.; Carter, W.B.; Schaedler, T.A. Additive manufacturing of polymer-derived ceramics. *Science* **2016**, *351*, 58–62. [CrossRef]

15. Jens, B.; Stefan, H.; Iwiza, T.; Ruth, S.; Oliver, K. High-strength cellular ceramic composites with 3D microarchitecture. *Proc. Natl. Acad. Sci. USA* **2014**, *111*, 2453–2458.

16. Ozdemir, Z.; Hernandez-Nava, E.; Tyas, A.; Warren, J.A.; Fay, S.D.; Goodall, R.; Todd, I.; Askes, H. Energy absorption in lattice structures in dynamics: Experiments. *Int. J. Impact. Eng.* **2016**, *89*, 49–61. [CrossRef]

17. Liu, Y.J.; Li, S.J.; Wang, H.L.; Hou, W.T.; Hao, Y.L.; Yang, R.; Sercombe, T.B.; Zhang, L.C. Microstructure, defects and mechanical behavior of beta-type titanium porous structures manufactured by electron beam melting and selective laser melting. *Acta Mater.* **2016**, *113*, 56–67. [CrossRef]

18. Qiu, C.; Yue, S.; Adkins, N.J.E.; Ward, M.; Hassanin, H.; Lee, P.D.; Withers, P.J.; Attallah, M.M. Influence of processing conditions on strut structure and compressive properties of cellular lattice structures fabricated by selective laser melting. *Mater. Sci. Eng. A* **2015**, *628*, 188–197. [CrossRef]

19. Yu, G.; Li, Z.; Li, S.; Zhang, Q.; Hua, Y.; Liu, H.; Zhao, X.; Dhaidhai, D.T.; Li, W.; Wang, X. The select of internal architecture for porous Ti alloy scaffold: A compromise between mechanical properties and permeability. *Mater. Des.* **2020**, *192*, 108754. [CrossRef]

20. Dallago, M.; Raghavendra, S.; Luchin, V.; Zappini, G.; Pasini, D.; Benedetti, M. The role of node fillet, unit-cell size and strut orientation on the fatigue strength of Ti-6Al-4V lattice materials additively manufactured via laser powder bed fusion. *Int. J. Fatigue* **2021**, *142*, 105946. [CrossRef]

21. Latture, R.M.; Rodriguez, R.X.; Holmes, L.R.; Zok, F.W. Effects of nodal fillets and external boundaries on compressive response of an octet truss. *Acta Mater.* **2018**, *149*, 78–87. [CrossRef]

22. Bai, L.; Yi, C.; Chen, X.; Sun, Y.; Zhang, J. Effective design of the graded strut of BCC lattice structure for improving mechanical properties. *Materials* **2019**, *12*, 2192. [CrossRef] [PubMed]

23. Liu, Y.; Zhang, J.; Gu, X.; Zhou, Y.; Yin, Y.; Tan, Q.; Li, M.; Zhang, M.-X. Mechanical performance of a node reinforced body-centred cubic lattice structure manufactured via selective laser melting. *Scr. Mater.* **2020**, *189*, 95–100. [CrossRef]

24. Zhang, Y.; Xu, X.; Fang, J.; Huang, W.; Wang, J. Load characteristics of triangular honeycomb structures with self-similar hierarchical features. *Eng. Struct.* **2022**, *257*, 114114. [CrossRef]

25. Roach, A.M.; White, B.C.; Garland, A.; Jared, B.H.; Carroll, J.D.; Boyce, B.L. Size-dependent stochastic tensile properties in additively manufactured 316L stainless steel. *Addit. Manuf.* **2020**, *32*, 101090. [CrossRef]

26. Li, P.; Wang, Z.; Petrinic, N.; Siviour, C.R. Deformation behaviour of stainless steel microlattice structures by selective laser melting. *Mater. Sci. Eng. A* **2014**, *614*, 116–121. [CrossRef]

27. Jiang, F.; Yang, S.; Qi, C. Quasi-static crushing response of a novel 3D re-entrant circular auxetic metamaterial. *Compos. Struct.* **2022**, *300*, 116066. [CrossRef]

28. Zhu, G.; Wen, D.; Wei, L.; Wang, Z.; Zhao, X. Mechanical performances of novel cosine function cell-based metallic lattice structures under quasi-static compressive loading. *Compos. Struct.* **2023**, *314*, 116962. [CrossRef]

29. Zhu, G.; Zhao, Z.; Cao, X.; Wei, L.; Wang, Z.; Zhao, X. On crushing behavior of square aluminum/CFRP hybrid structures subjected to quasi-static loading. *Thin-Walled Struct.* **2023**, *184*, 110486. [CrossRef]

30. Li, P.; Yang, F.; Bian, Y.; Zhang, S.; Wang, L. Designable mechanical properties of modified body-centered cubic lattice materials. *Compos. Struct.* **2023**, *317*, 117060. [CrossRef]

31. Yao, S.; Zhou, Y.; Li, Z.; Zhang, P.; Cao, Y.; Xu, P. Energy absorption characteristics of square frustum lattice structure. *Compos. Struct.* **2021**, *275*, 114492. [CrossRef]

32. Ha, N.S.; Pham, T.M.; Tran, T.T.; Hao, H.; Lu, G. Mechanical properties and energy absorption of bio-inspired hierarchical circular honeycomb. *Compos. B Eng.* **2022**, *236*, 109818. [CrossRef]

33. Tabacu, S. Axial crushing of circular structures with rectangular multi-cell insert. *Thin-Walled Struct.* **2015**, *95*, 297–309. [CrossRef]

34. Li, Z.; Yao, S.; Ma, W.; Xu, P.; Che, Q. Energy-absorption characteristics of a circumferentially corrugated square tube with a cosine profile. *Thin-Walled Struct.* **2019**, *135*, 385–399. [CrossRef]

35. Yang, J.; Chen, X.; Sun, Y.; Zhang, J.; Feng, C.; Wang, Y.; Wang, K.; Bai, L. Compressive properties of bidirectionally graded lattice structures. *Mater. Des.* **2022**, *218*, 110683. [CrossRef]

36. Sharma, D.; Hiremath, S.S. Bio-inspired repeatable lattice structures for energy absorption: Experimental and finite element study. *Compos. Struct.* **2022**, *283*, 115102. [CrossRef]

37. Jia, H.; Lei, H.; Wang, P.; Meng, J.; Li, C.; Zhou, H.; Zhang, X.; Fang, D. An experimental and numerical investigation of compressive response of designed Schwarz Primitive triply periodic minimal surface with non-uniform shell thickness. *Extreme Mech. Lett.* **2020**, *37*, 100671. [CrossRef]

38. Rodrigo, C.; Xu, S.; Durandet, Y.; Fraser, D.; Ruan, D. Quasi-static and dynamic compression of additively manufactured functionally graded lattices: Experiments and simulations. *Eng. Struct.* **2023**, *284*, 115909. [CrossRef]

39. Gibson, L.J.; Ashby, M.F. *Cellular Solids: Structure and Properties*; Cambridge University Press: Cambridge, UK, 1997.

40. Bai, L.; Gong, C.; Chen, X.; Zheng, J.; Yang, J.; Li, K.; Sun, Y. Heterogeneous compressive responses of additively manufactured Ti-6Al-4V lattice structures by varying geometric parameters of cells. *Int. J. Mech. Sci.* **2022**, *214*, 106922. [CrossRef]

41. Li, C.; Lei, H.; Zhang, Z.; Zhang, X.; Zhou, H.; Wang, P.; Fang, D. Architecture design of periodic truss-lattice cells for additive manufacturing. *Addit. Manuf.* **2020**, *34*, 101172. [CrossRef]

42. Beharic, A.; Rodriguez Egui, R.; Yang, L. Drop-weight impact characteristics of additively manufactured sandwich structures with different cellular designs. *Mater. Des.* **2018**, *145*, 122–134. [CrossRef]